Surface enhanced Raman scattering in the presence of multilayer dielectric structures

Aida Delfan,[1],* Marco Liscidini,[2] and John E. Sipe[1]

[1]*Department of Physics and Institute for Optical Sciences, University of Toronto, 60 St. George Street, Ontario M5S 1A7, Canada*
[2]*Department of Physics, University of Pavia, Via Bassi 6, I-27100 Pavia, Italy*
**Corresponding author: adelfan@physics.utoronto.ca*

Received April 16, 2012; accepted May 10, 2012;
posted May 24, 2012 (Doc. ID 166667); published July 3, 2012

We perform a systematic study of spontaneous Raman scattering in resonant planar structures. We present a semiclassical approach that allows the description of spontaneous Raman scattering in an arbitrary multilayer, providing analytical expressions of the Raman cross sections in terms of the Fresnel coefficients of the structure and taking into account beam size effects. Large enhancements of the Raman cross section are predicted in fully dielectric structures. In particular, given our results, truncated periodic multilayers supporting Bloch surface waves might be of interest for the realization of integrated Raman sensor devices. © 2012 Optical Society of America

OCIS codes: 240.6695, 240.6690, 280.4788, 310.2785.

1. INTRODUCTION

Raman scattering is a powerful spectroscopic tool for molecular identification. It offers high selectivity, with the Raman spectrum serving as a fingerprint of the detected molecule. Although this scattering process is usually very weak, with typical cross sections of about 10^{-30} cm^2 molecule^{-1} sr^{-1} [1], it can be enhanced when molecules are located in the proximity of roughened metallic surfaces [2–4], nanoparticles in a solution [2,3,5], or nanoparticles on a substrate [6–9]. This surface enhanced Raman scattering (SERS) relies in large part on the coupling of the incident and scattered fields through localized surface plasmon (SP) resonances [2]. While typical average SERS enhancement factors are about 10^6, enhancements of about 10^{14} for dye molecules at "hot spots" on aggregated gold and silver nanoparticles have been observed [10,11], enabling single molecule spectroscopy. Other SERS structures include periodic arrays of metallic nanoparticles [12,13] or holes in metallic films [12,14] and metallic gratings [15]; photonic crystal fibers with metal coatings and metal nanoparticles have also been used [16].

A dielectric waveguide (WG) structure, supporting confined modes, leads to field enhancement at the positions of adsorbed molecules, and thus to SERS, as well. Slab WGs can lead to enhancements of about 3 orders of magnitude [17–20], and have been used to study Raman scattering from thin polymer films [21], monolayers of proteins [22], and bacteriorhodopsin [23]. Coupled WGs have also been used to study the Raman scattering from a thin liquid film between them [24].

Sensing scenarios employing these structures typically involve coupling into the WG mode by a prism in the Otto configuration [25], and detecting light scattered out of the WG structure. In this paper we theoretically study SERS from molecules adsorbed on structures and probed in the Kretschmann configuration [26]. While this configuration has been widely employed in biosensing based on changes in the refractive index [2,27], to the best of our knowledge, no Raman scattering in dielectric planar structures based on the Kretschmann configuration has been reported [28]. In the Kretschmann configuration, the scattered signal is detected through a prism substrate, reducing the interaction of the scattered field with the solution containing the analyte; as well, microfluidic systems for the delivery of the analytes are easily envisioned. Moreover, this configuration allows for coupling of the scattered field into guided modes of the planar structure, which we show further enhances radiation in specific directions; this may be important for extensions to multiplexing.

Besides studying slab WG structures in the Kretschmann configuration, we also consider the use of Bloch surface waves (BSWs) [29,30], which propagate at the surface of periodic dielectric stacks [one-dimensional (1D) photonic crystals]. These waves are confined to the surface of the structure due to the photonic bandgap from the photonic crystal and total internal reflection from the cladding. They can be seen as dielectric analogues of planar SP structures, but do not suffer from absorption losses, and are of interest for sensing and biosensing applications [31–37]. BSW structures can be designed to have very narrow resonance peaks, and their dispersion relations can be widely tuned by changing the parameters of the multilayers. Thus they offer more flexibility for sensing optimization than usual slab WGs.

The paper is organized as follows. As a benchmark, we begin in Subsection 2.A by calculating the Raman cross section for a molecule embedded in a uniform background medium, adopting a simple isotropic model for the Raman polarizability. Although in a design study for a particular sensing application this would have to be replaced by a more realistic model, the simple isotropic model allows us to focus on the enhancement of the Raman scattering in the different planar geometries we consider. In Subsection 2.B, we describe the Raman scattering from a molecule over a very general

0740-3224/12/081863-12$15.00/0

multilayer structure, identifying expressions for the Raman scattering into the cladding and substrate. We cast the results in terms involving the Fresnel coefficients of the structure. This allows for an identification of any guided modes, and the construction of approximate analytic expressions characterizing their effects, as well as the implementation of numerical calculations. In Section 3, we turn to example calculations involving particular multilayer structures. Besides WG and BSW structures, we also consider planar SP structures. While these are not the best metallic structures for SERS, they provide an indication of what Raman signal enhancement could be achieved with the kind of planar SP structures commonly used in biosensing [2,27]. All these calculations employ a plane wave analysis, which can be suspect with resonant structures. In Section 4, we generalize our results to excitation with finite beams, see how the limit of plane wave excitation arises, and identify when corrections to it become important. In Section 5, we present our conclusions.

2. RAMAN CROSS SECTION

We calculate spontaneous Raman scattering within a semiclassical approximation: The incident field is taken as classical, but we treat the vibrations in the molecule quantum mechanically. All optical fields are taken to be at frequencies far below any electronic resonances, so we can describe the response of the molecule to incident radiation by a polarizability tensor $\boldsymbol{\alpha}(t)$, which is modulated by molecular vibration. The dipole moment $\boldsymbol{\mu}(t) = \boldsymbol{\alpha}(t) \cdot \boldsymbol{E}(t)$, where $\boldsymbol{E}(t)$ is the field at the position of the molecule resulting from the incident beam. In our approach, $\boldsymbol{\mu}(t)$ is an operator by virtue of its dependence on the molecular vibration through $\boldsymbol{\alpha}(t)$. Thus the radiated fields are operators, too, and we calculate the scattered light by taking the expectation value of the resulting Poynting vector operator. This allows us to capture the correct intensities of Stokes and anti-Stokes radiation.

We take the polarizability tensor to be of the form

$$\boldsymbol{\alpha}(t) = \boldsymbol{\alpha}_0 + \sum_{\xi} \boldsymbol{\alpha}_{1\xi} q^{\xi}(t), \tag{1}$$

where $\boldsymbol{\alpha}_0$ and $\boldsymbol{\alpha}_{1\xi}$ are, respectively, the Rayleigh polarizability tensor and the Raman polarizability tensor associated with the vibrational degree of freedom ξ; $q^{\xi}(t)$ is the canonical coordinate associated with this degree of freedom. Since our main concern here is the enhancement of Raman scattering that can result from the use of multilayer structures, and not the detailed description of the Raman scattering from a particular molecule, we consider only 1 degree of freedom, and model the vibration as a harmonic oscillator at frequency ω_0. We consider only spontaneous processes and, ignoring the details of the frequency width of the Raman lines due to coupling of the molecule with environmental degrees of freedom, we take

$$q(t) = \left(\frac{\hbar}{2m\omega_0}\right)^{1/2} (a e^{-i\omega_0 t} + a^{\dagger} e^{i\omega_0 t}), \tag{2}$$

where a and $a^{\dagger}$ are the lowering and raising operators of the harmonic oscillator, respectively. We now denote the single Raman polarizability tensor simply by $\boldsymbol{\alpha}_1$; to simplify the calculations, we treat the Raman polarizability as isotropic, with $\boldsymbol{\alpha}_1$ proportional to the unit tensor, and denote the proportionality constant by α_1. Generalization to treat more realistic polarizability tensors is straightforward.

A. Molecule in a Uniform Medium

We begin with a molecule embedded in a uniform medium with real refractive index $n_1(\omega)$ and subject to a continuous wave incident pump field at frequency ω_P; we make calculations by assuming an incident pump pulse with duration T:

$$\boldsymbol{E}_{\text{inc}}(t) = \begin{cases} \boldsymbol{\mathcal{E}} e^{-i\omega_P t} + c.c & -T/2 < t < T/2, \\ 0 & \text{otherwise}, \end{cases} \tag{3}$$

where $\boldsymbol{E}_{\text{inc}}(t)$ is the electric field at the position of the molecule, and finally take the limit $T \to \infty$. For all fields $f(t)$, we introduce positive and negative frequency parts

$$f^{\pm}(t) = \int_{-\infty}^{\infty} \frac{\mathrm{d}\omega}{2\pi} f^{\pm}(\omega) e^{-i\omega t}, \tag{4}$$

where $f^{\pm}(\omega) = \theta(\pm\omega) f(\omega)$, with $\theta(s) = 1, 0$ as $s > 0$, $s < 0$, and

$$f(\omega) = \int_{-\infty}^{\infty} f(t) e^{-i\omega t} \mathrm{d}t. \tag{5}$$

Then, for $\omega_P \gg \omega_0$, to good approximation, the positive frequency component $\boldsymbol{\mu}^{+}(\omega)$ of the dipole moment operator is related to the positive frequency components of the incident field:

$$\boldsymbol{\mu}^{+}(\omega) = \left(\frac{\hbar}{2m\omega_0}\right)^{1/2} \alpha_1 (a \boldsymbol{E}^{+}_{\text{inc}}(\omega - \omega_0) + a^{\dagger} \boldsymbol{E}^{+}_{\text{inc}}(\omega + \omega_0)), \tag{6}$$

where we neglect Rayleigh scattering. The fields radiated by this resulting dipole moment can be found from the usual solutions [38] of the Maxwell equations:

$$\begin{aligned} \boldsymbol{E}^{+}(\boldsymbol{r}, \omega) &= \frac{\tilde{\omega}^2}{4\pi\epsilon_0} \frac{e^{i\tilde{\omega} n_1 r}}{r} (\hat{\boldsymbol{r}} \times \boldsymbol{\mu}^{+}(\omega)) \times \hat{\boldsymbol{r}}, \\ \boldsymbol{H}^{+}(\boldsymbol{r}, \omega) &= \frac{\tilde{\omega}^2 n_1 c}{4\pi} \frac{e^{i\tilde{\omega} n_1 r}}{r} (\hat{\boldsymbol{r}} \times \boldsymbol{\mu}^{+}(\omega)), \end{aligned} \tag{7}$$

where c is the speed of light and $\tilde{\omega} = \omega/c$ is the (circular) wavenumber. The quantities $\boldsymbol{E}^{+}(\boldsymbol{r}, \omega)$ and $\boldsymbol{H}^{+}(\boldsymbol{r}, \omega)$ are operators, by virtue of the fact that $\boldsymbol{\mu}^{+}(\omega)$ is an operator. The part of the Poynting vector operator, $\boldsymbol{S}(\boldsymbol{r}, t) = \boldsymbol{E}(\boldsymbol{r}, t) \times \boldsymbol{H}(\boldsymbol{r}, t)$, that will be important for the interaction of the radiation with detectors is the normally ordered form [39]

$$: \boldsymbol{S}(\boldsymbol{r}, t) : \equiv \boldsymbol{E}^{-}(\boldsymbol{r}, t) \times \boldsymbol{H}^{+}(\boldsymbol{r}, t) - \boldsymbol{H}^{-}(\boldsymbol{r}, t) \times \boldsymbol{E}^{+}(\boldsymbol{r}, t), \tag{8}$$

and integrating over time and using Eq. (4),

$$\int_{-\infty}^{\infty} : \boldsymbol{S}(\boldsymbol{r}, t) : \mathrm{d}t = \int_{0}^{\infty} \boldsymbol{\mathcal{S}}(\boldsymbol{r}, \omega) \mathrm{d}\omega, \tag{9}$$

where

$$\boldsymbol{\mathcal{S}}(\boldsymbol{r}, \omega) = \frac{1}{2\pi} ((\boldsymbol{E}^{+}(\boldsymbol{r}, \omega))^{\dagger} \times \boldsymbol{H}^{+}(\boldsymbol{r}, \omega) - (\boldsymbol{H}^{+}(\boldsymbol{r}, \omega))^{\dagger} \times \boldsymbol{E}^{+}(\boldsymbol{r}, \omega)), \tag{10}$$

is the operator for the radiated energy per area per unit frequency interval at position $\mathbf{r}$. From Eqs. (7) and 10,

$$\mathcal{S}(\mathbf{r},\omega) = \frac{\tilde{\omega}^4 n_1 c}{16\pi^3\epsilon_0}\frac{\hat{\mathbf{r}}}{r^2}\Gamma_{\text{free}}(\hat{\mathbf{r}}) : (\boldsymbol{\mu}^+(\omega))^\dagger\boldsymbol{\mu}^+(\omega), \tag{11}$$

where $\Gamma^{ij}_{\text{free}}(\hat{\mathbf{r}}) = \delta^{ij} - r^i r^j/r^2$, and the colon product of tensor T and vectors $\mathbf{A}$ and $\mathbf{B}$ is defined as $T : \mathbf{AB} = T^{ij}A^iB^j$. The expectation value of $\mathcal{S}(\mathbf{r},\omega)$ is

$$\langle\mathcal{S}(\mathbf{r},\omega)\rangle = \frac{\tilde{\omega}^4 n_1 c}{16\pi^3\epsilon_0}\frac{\hat{\mathbf{r}}}{r^2}\Gamma_{\text{free}}(\hat{\mathbf{r}}) : \langle(\boldsymbol{\mu}^+(\omega))^\dagger\boldsymbol{\mu}^+(\omega)\rangle. \tag{12}$$

From Eqs. (6) and (3), in the limit $(\omega_P T \gg 1)$, we find

$$\begin{aligned}\frac{\langle\boldsymbol{\mu}^+(\omega))^\dagger\boldsymbol{\mu}^+(\omega)\rangle}{T} &= \frac{\pi(\alpha_1\ell_A)^2}{2}\boldsymbol{\mathcal{E}}^*\boldsymbol{\mathcal{E}}\delta(\omega-\omega_P-\omega_0)\\ &\quad+\frac{\pi(\alpha_1\ell_S)^2}{2}\boldsymbol{\mathcal{E}}^*\boldsymbol{\mathcal{E}}\delta(\omega-\omega_P+\omega_0),\end{aligned} \tag{13}$$

where

$$\ell_S = \sqrt{\left(\frac{\hbar}{2m\omega_0}\right)(\bar{n}+1)}, \qquad \ell_A = \sqrt{\left(\frac{\hbar}{2m\omega_0}\right)\bar{n}}, \tag{14}$$

are characteristic lengths associated with Stokes and anti-Stokes radiation, respectively, ($\bar{n} = (e^{\hbar\omega_0/k_BT}-1)^{-1}$ is the average number of the vibrational excitations). When the temperature approaches zero, ℓ_A vanishes, and ℓ_S characterizes the length associated with the zero-point motion of the oscillator; on the contrary, when $k_BT \gg \hbar\omega$, ℓ_A and ℓ_S become equal and characterize the length associated with the thermal motion of the oscillator.

The radiated energy per unit area per time at position $\mathbf{r}$ is

$$\begin{aligned}\frac{1}{T}\int_0^\infty\langle\mathcal{S}(\mathbf{r},\omega)\rangle d\omega &= \frac{\tilde{\omega}_S^4 n_1(\omega_S)c}{32\pi^2\epsilon_0}(\alpha_1\ell_S)^2\frac{\hat{\mathbf{r}}}{r^2}\boldsymbol{\Gamma}_{\text{free}}(\hat{\mathbf{r}},\omega_S) : (\boldsymbol{\mathcal{E}}^*\boldsymbol{\mathcal{E}})\\ &\quad+\frac{\tilde{\omega}_A^4 n_1(\omega_A)c}{32\pi^2\epsilon_0}(\alpha_1\ell_A)^2\frac{\hat{\mathbf{r}}}{r^2}\boldsymbol{\Gamma}_{\text{free}}(\hat{\mathbf{r}},\omega_A)\\ &\quad: (\boldsymbol{\mathcal{E}}^*\boldsymbol{\mathcal{E}}),\end{aligned} \tag{15}$$

where $\omega_S = \omega_P - \omega_0$ and $\omega_A = \omega_P + \omega_0$ are the Stokes and anti-Stokes frequencies, and the first and second terms correspond to the Stokes $\langle\mathbf{S}_S(\mathbf{r})\rangle$ and anti-Stokes $\langle\mathbf{S}_A(\mathbf{r})\rangle$ radiation, respectively. If we consider only the Stokes field, the total power radiated at ω_S is given by

$$P_S = \int\langle\mathbf{S}_S(\mathbf{r})\rangle\cdot\hat{\mathbf{r}}r^2 d\Omega = \frac{\tilde{\omega}_S^4 n_1(\omega_S)c}{12\pi\epsilon_0}(\alpha_1\ell_S)^2\boldsymbol{\mathcal{E}}^*\cdot\boldsymbol{\mathcal{E}}, \tag{16}$$

where we integrated $\langle\mathbf{S}_S(\mathbf{r})\rangle$ over the solid angle Ω. We can define the Stokes Raman differential cross section in a uniform medium as

$$\sigma_S^o(\hat{\mathbf{r}}) = \frac{\langle\mathbf{S}_S(\mathbf{r})\rangle\cdot\hat{\mathbf{r}}r^2}{S_P}, \tag{17}$$

where

$$S_P = \frac{2n_1(\omega_P)}{c\mu_0}(\boldsymbol{\mathcal{E}}^*\cdot\boldsymbol{\mathcal{E}}), \tag{18}$$

is the magnitude of the Poynting vector of the pump field. We obtain

$$\sigma_S^o(\hat{\mathbf{r}}) \equiv \frac{\tilde{\omega}_S^4 n_1(\omega_S)}{4n_1(\omega_P)}\left(\frac{\alpha_1\ell_S}{4\pi\epsilon_0}\right)^2\boldsymbol{\Gamma}_{\text{free}}(\hat{\mathbf{r}},\omega_S) : (\hat{\mathbf{e}}^*_{\text{inc}}\hat{\mathbf{e}}_{\text{inc}}), \tag{19}$$

where we assume that the incident field is polarized along $\hat{e}_{\text{inc}}$. Finally, the total Raman cross section is found by integrating $\sigma_S^o(\hat{\mathbf{r}})$ over the solid angle:

$$\sigma_S^o = \int\sigma_S^o(\hat{\mathbf{r}})d\Omega = \frac{2\pi\tilde{\omega}_S^4 n_1(\omega_S)}{3n_1(\omega_P)}\left(\frac{\alpha_1\ell_S}{4\pi\epsilon_0}\right)^2. \tag{20}$$

Similar results for the radiated power and the differential cross section are obtained for the anti-Stokes radiation.

B. Molecule Above a Planar Structure

Now we turn to the problem of interest (see Fig. 1). A molecule is embedded in a medium of real refractive index $n_1(\omega)$ at a distance d above a planar structure oriented with a normal vector $\hat{z}$ and extending from $z = 0$ to $z = D$, with a uniform substrate medium with real refractive index $n_N(\omega)$ for $z < 0$; we take the position of the molecule to be $\mathbf{r}_0 = (d+D)\hat{z} + \mathbf{R}_0$, where $\mathbf{R}_0 = (x_0, y_0)$. We consider a configuration in which the pump beam is incident from the substrate, such that the field at the position of the molecule, $\mathbf{E}_L(t)$, is

$$\mathbf{E}_L(t) = \begin{cases}\boldsymbol{\mathcal{E}}_L e^{-i\omega_P t} + c.c & -T/2 < t < T/2,\\ 0 & \text{otherwise.}\end{cases} \tag{21}$$

In analogy to Eq. (6), we can write down the expression for the induced dipole moment of the molecule

$$\boldsymbol{\mu}^+(\omega) = \left(\frac{\hbar}{2m\omega_0}\right)^{1/2}\alpha_1(a\mathbf{E}_L^+(\omega-\omega_0) + a^\dagger\mathbf{E}_L^+(\omega+\omega_0)). \tag{22}$$

The fields radiated by the dipole are modified in the presence of the structure [40]. In particular, in the cladding,

$$\mathbf{E}^+(\mathbf{r},\omega) = \int\frac{i d\boldsymbol{\kappa}}{2\pi w_1}\mathbf{e}_1(\boldsymbol{\kappa},\omega)e^{i\boldsymbol{\nu}_{1+}\cdot\mathbf{r}}, \tag{23}$$

where $\boldsymbol{\nu}_{1+}$ is the wave vector and, in general,

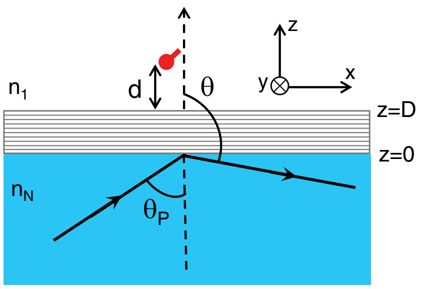

Fig. 1. (Color online) Sketch of the pump and detection configuration under consideration in the case of spontaneous Raman scattering, θ_P is the incident angle of the pump in the substrate.

$$\boldsymbol{\nu}_{i\pm} \equiv \boldsymbol{\kappa} \pm w_i \hat{\mathbf{z}}, \tag{24}$$

with

$$\boldsymbol{\kappa} = \kappa_x \hat{\mathbf{x}} + \kappa_y \hat{\mathbf{y}}, \tag{25}$$

where κ_x and κ_y are real, and

$$w_i = \sqrt{(n_i \tilde{\omega})^2 - \kappa^2}, \tag{26}$$

with the square root convention that $\mathrm{Im}\sqrt{z} \geq 0$, and if $\mathrm{Im}\sqrt{z} = 0$, then $\mathrm{Re}\sqrt{z} \geq 0$. The subscript i refers to the medium in which the quantities are calculated, where 1 and N indicate cladding and substrate, respectively, and $+/-$ corresponds to upward/downward propagating fields. Finally,

$$\mathbf{e}_1(\boldsymbol{\kappa}, \omega) = \frac{\tilde{\omega}^2}{4\pi\epsilon_0}(\hat{\mathbf{s}}\boldsymbol{\gamma}_{s1}(\boldsymbol{\kappa}, \omega) + \hat{\mathbf{p}}_{1+}\boldsymbol{\gamma}_{p1}(\boldsymbol{\kappa}, \omega)) \cdot \boldsymbol{\mu}^{+}(\omega), \tag{27}$$

with

$$\begin{aligned} \boldsymbol{\gamma}_{s1}(\boldsymbol{\kappa}, \omega) &= (e^{-iw_1 d} + e^{iw_1 d} R_{1N}^{s})\hat{\mathbf{s}}, \\ \boldsymbol{\gamma}_{p1}(\boldsymbol{\kappa}, \omega) &= (e^{-iw_1 d}\hat{\mathbf{p}}_{1+} + e^{iw_1 d} R_{1N}^{p}\hat{\mathbf{p}}_{1-}), \end{aligned} \tag{28}$$

where the unit polarization vectors of the radiated field in medium 1, $\hat{\mathbf{s}}$ and $\hat{\mathbf{p}}_{1+}$ are defined according to

$$\hat{\mathbf{s}} = \hat{\boldsymbol{\kappa}} \times \hat{\mathbf{z}}, \qquad \hat{\mathbf{p}}_{i\pm} = \frac{\kappa\hat{\mathbf{z}} \mp w_i \hat{\boldsymbol{\kappa}}}{\nu_i}, \tag{29}$$

and R_{1N}^{s} and R_{1N}^{p} are the Fresnel reflection coefficients (from the cladding to the substrate) for s and p polarizations, respectively, with $\nu_i \equiv \sqrt{\boldsymbol{\nu}_i^{*} \cdot \boldsymbol{\nu}_i}$. As we are interested in the far-field radiation, we consider the asymptotic limit $r \to \infty$ for a fixed $\hat{\mathbf{r}}$. We expect the far-field radiation to be dominated by the contribution associated with the wave vector that is exactly in the direction of $\hat{\mathbf{r}}$. This is indeed the case [40], and the field [Eq. (23)] in the cladding, far from the dipole source, is given by

$$\mathbf{E}^{+}(\mathbf{r}, \omega) \sim \frac{\tilde{\omega}^2}{4\pi\epsilon_0}(\bar{\hat{\mathbf{s}}}\boldsymbol{\gamma}_{s1}(\bar{\boldsymbol{\kappa}}, \omega) + \bar{\hat{\mathbf{p}}}_{1+}\boldsymbol{\gamma}_{p1}(\bar{\boldsymbol{\kappa}}, \omega)) \cdot \boldsymbol{\mu}^{+}(\omega)\frac{e^{i\tilde{\omega}n_1 r}}{r}, \tag{30}$$

and

$$\mathbf{H}^{+}(\mathbf{r}, \omega) \sim \frac{n_1 c\tilde{\omega}^2}{4\pi}(\bar{\hat{\mathbf{s}}}\boldsymbol{\gamma}_{p1}(\bar{\boldsymbol{\kappa}}, \omega) - \bar{\hat{\mathbf{p}}}_{1+}\boldsymbol{\gamma}_{s1}(\bar{\boldsymbol{\kappa}}, \omega)) \cdot \boldsymbol{\mu}^{+}(\omega)\frac{e^{i\tilde{\omega}n_1 r}}{r}, \tag{31}$$

where $\bar{\boldsymbol{\kappa}} = \tilde{\omega}n_1(\hat{\mathbf{x}}\hat{\mathbf{x}} + \hat{\mathbf{y}}\hat{\mathbf{y}}) \cdot \hat{\mathbf{r}}$, and the bars on each quantity indicate its evaluation at $\bar{\boldsymbol{\kappa}}$. By inserting Eqs. (30) and (31) into Eq. (10), we obtain the Stokes radiation per time per unit area in the cladding at $\mathbf{r}$:

$$\langle \mathbf{S}_S(\mathbf{r}) \rangle = \frac{\tilde{\omega}_S^4 n_1(\omega_S) c}{32\pi^2\epsilon_0}(\alpha_1 \ell_S)^2 \frac{\hat{\mathbf{r}}}{r^2}\boldsymbol{\Gamma}_{\mathrm{clad}}(\hat{\mathbf{r}}, \omega_S) : (\boldsymbol{\mathcal{E}}_L^{*}\boldsymbol{\mathcal{E}}_L), \tag{32}$$

with

$$\boldsymbol{\Gamma}_{\mathrm{clad}}(\hat{\mathbf{r}}, \omega_S) = \boldsymbol{\gamma}_{s1}^{*}(\bar{\boldsymbol{\kappa}}, \omega_S)\boldsymbol{\gamma}_{s1}(\bar{\boldsymbol{\kappa}}, \omega_S) + \boldsymbol{\gamma}_{p1}^{*}(\bar{\boldsymbol{\kappa}}, \omega_S)\boldsymbol{\gamma}_{p1}(\bar{\boldsymbol{\kappa}}, \omega_S). \tag{33}$$

We can now relate $\langle \mathbf{S}_S(\mathbf{r}) \rangle$ to the field incident from the substrate. We take that field to be

$$\mathbf{E}_{\mathrm{inc}}(\mathbf{r}, t) = \boldsymbol{\mathcal{E}} e^{i\boldsymbol{\kappa}^P \cdot \mathbf{R}} e^{iw_N^P z} e^{-i\omega_P t} + c.c, \tag{34}$$

within our time window T [Eq. (21)], where $\mathbf{R} = (x, y)$; the superscript P on a quantity indicates evaluation for the pump beam. Here $\mathcal{E} = \mathcal{E}\hat{\mathbf{e}}_{\mathrm{inc}} = (F_s\hat{\mathbf{s}}^P + F_p\hat{\mathbf{p}}_{N+}^P)\mathcal{E}$, where F_s and F_p indicate the s- and p-polarized components of the incident beam, $|F_s|^2 + |F_p|^2 = 1$. Then the field at the position of the molecule is specified by

$$\boldsymbol{\mathcal{E}}_L = \mathbf{e}_L(\boldsymbol{\kappa}^P, \omega_P)\boldsymbol{\mathcal{E}} e^{i\boldsymbol{\kappa}^P \cdot \mathbf{R}_0}, \tag{35}$$

with

$$\mathbf{e}_L(\boldsymbol{\kappa}^P, \omega_P) = (T_{N1}^{s}(\kappa^P, \omega_P)F_s\hat{\mathbf{s}}^P + T_{N1}^{p}(\kappa^P, \omega_P)F_p\hat{\mathbf{p}}_{1+}^P)e^{iw_1^P d}, \tag{36}$$

where T_{N1}^{s} and T_{N1}^{p} are the Fresnel transmission coefficients for s and p polarizations, respectively. From Eqs. (35) and (32) we obtain

$$\langle \mathbf{S}_S(\mathbf{r}) \rangle = \frac{\tilde{\omega}_S^4 n_1(\omega_S) c|\mathcal{E}|^2}{32\pi^2\epsilon_0}(\alpha_1 \ell_S)^2 \frac{\hat{\mathbf{r}}}{r^2}\boldsymbol{\Gamma}_{\mathrm{clad}}(\hat{\mathbf{r}}, \omega_S) : (\mathbf{e}_L^{*}\mathbf{e}_L). \tag{37}$$

Analogous to Eq. (17), we can define the Stokes cross section for the molecules on planar structures as

$$\sigma_S(\hat{\mathbf{r}}) = \frac{\langle \mathbf{S}_S(\mathbf{r}) \rangle \cdot \hat{\mathbf{r}} r^2}{S_P}, \tag{38}$$

where

$$S_P = \frac{2n_N(\omega_P)}{c\mu_0}(\boldsymbol{\mathcal{E}}^{*} \cdot \boldsymbol{\mathcal{E}}). \tag{39}$$

Thus, the differential Stokes cross section for the radiation into the cladding becomes

$$\sigma_S(\hat{\mathbf{r}}) = \frac{\tilde{\omega}_S^4 n_1(\omega_S)}{4n_N(\omega_P)}\left(\frac{\alpha_1 \ell_S}{4\pi\epsilon_0}\right)^2 \boldsymbol{\Gamma}_{\mathrm{clad}}(\hat{\mathbf{r}}, \omega_S) : (\mathbf{e}_L^{*}\mathbf{e}_L). \tag{40}$$

It is convenient to introduce a normalized differential cross section, $\bar{\sigma}_S(\hat{\mathbf{r}})$, by dividing $\sigma_S(\hat{\mathbf{r}})$ by the total cross section calculated assuming the molecule is embedded in a uniform medium of index $n_1(\omega)$:

$$\bar{\sigma}_S(\hat{\mathbf{r}}) = \frac{\sigma_S(\hat{\mathbf{r}})}{\sigma_S^o} = \frac{3n_1(\omega_P)}{8\pi n_N(\omega_P)}\boldsymbol{\Gamma}_{\mathrm{clad}}(\hat{\mathbf{r}}, \omega_S) : (\mathbf{e}_L^{*}\mathbf{e}_L). \tag{41}$$

From Eqs. (33), (36), and (41) we have

$$\bar{\sigma}_S(\hat{\mathbf{r}}) = \frac{3}{8\pi}\frac{n_1(\omega_P)}{n_N(\omega_P)}(|\boldsymbol{\gamma}_{s1}(\bar{\boldsymbol{\kappa}}, \omega_S).\mathbf{e}_L|^2 + |\boldsymbol{\gamma}_{p1}(\bar{\boldsymbol{\kappa}}, \omega_S).\mathbf{e}_L|^2). \tag{42}$$

For an arbitrary $\bar{\boldsymbol{\kappa}}$, we take ϕ to be the angle $\bar{\boldsymbol{\kappa}}$ makes with $\hat{\boldsymbol{\kappa}}^P$, such that

$$\bar{\hat{\boldsymbol{s}}} = \hat{\boldsymbol{s}}^P \cos\phi + \hat{\boldsymbol{\kappa}}^P \sin\phi, \qquad \bar{\hat{\boldsymbol{\kappa}}} = -\hat{\boldsymbol{s}}^P \sin\phi + \hat{\boldsymbol{\kappa}}^P \cos\phi. \tag{43}$$

Then the normalized differential cross section [Eq. (41)], which contains several inner products, will be a function of ϕ and θ, where θ is the angle between $\hat{\boldsymbol{r}}$ and $\hat{\boldsymbol{z}}$ (see Fig. 1). In a typical experimental setup, a detector will average only over a small range of θ and ϕ. In planar structures, the dependence on ϕ arises largely from the nature of the Raman tensor. We have taken a simple model of an isotropic Raman polarizability; the resulting ϕ dependence of the Raman signal will thus be weak and unrealistically small because of the choice of our simple model, chosen to focus on the effect of the resonances of a planar structure, which have their main dependence on θ. To concentrate on this latter dependence in a simple way, we focus on the integral of the differential cross section over ϕ:

$$\bar{\sigma}_{\text{clad}}(\theta) = \int_0^{2\pi} \bar{\sigma}_S(\hat{\boldsymbol{r}})\mathrm{d}\phi, \tag{44}$$

which gives

$$\begin{aligned}\bar{\sigma}_{\text{clad}}(\theta) = \frac{3}{8}\frac{n_1^P}{n_N^P}\Bigg(& \left|(1+e^{2iw_1 d}R_{1N}^s)T_{N1}^{sP}F_s e^{i(w_1^P - w_1)d}\right|^2 \\ & + \left|(1+e^{2iw_1 d}R_{1N}^s)\frac{w_1^P}{\tilde{\omega}^P n_1^P}T_{N1}^{pP}F_p e^{i(w_1^P - w_1)d}\right|^2 \\ & + 2\left|\frac{\kappa}{\tilde{\omega}n_1}(1+e^{2iw_1 d}R_{1N}^p)\frac{\kappa^P}{\tilde{\omega}^P n_1^P}T_{N1}^{pP}F_p e^{i(w_1^P - w_1)d}\right|^2 \\ & + \left|\frac{w_1}{\tilde{\omega}n_1}(1-e^{2iw_1 d}R_{1N}^p)\frac{w_1^P}{\tilde{\omega}^P n_1^P}T_{N1}^{pP}F_p e^{i(w_1^P - w_1)d}\right|^2 \\ & + \left|\frac{w_1}{\tilde{\omega}n_1}(1-e^{2iw_1 d}R_{1N}^p)T_{N1}^{sP}F_s e^{i(w_1^P - w_1)d}\right|^2\Bigg). \end{aligned} \tag{45}$$

Other than the quantities evaluated at $\boldsymbol{\kappa}^P$ and ω_P, as indicated by the superscript P, all quantities are evaluated at $\bar{\boldsymbol{\kappa}}$ and ω_S. Equation (45) describes the azimuthally integrated differential Stokes cross section for radiation into the cladding in terms of the Fresnel coefficients of the structure, which can be numerically calculated using the transfer matrix method [41]. The result is a sum of several terms, which depend on the fraction of the incident intensity that is transmitted through the structure multiplied by that fraction scattered into the cladding, which includes the direct scattered amplitude as well as the reflected scattered amplitude from the structure. The total normalized Stokes cross section for the radiation into the cladding is found by integrating $\bar{\sigma}_{\text{clad}}(\theta)$ over the angle θ:

$$\bar{\sigma}_{\text{clad}}^{\text{tot}} = \int_0^{\pi/2} \bar{\sigma}_{\text{clad}}(\theta)\sin(\theta)\mathrm{d}\theta. \tag{46}$$

The Stokes cross section for the radiation into the substrate can be found following the same approach. Analogous to Eqs. (30) and (31), the radiated electromagnetic fields into the substrate are [40]

$$\boldsymbol{E}^+(\boldsymbol{r},\omega) \sim \frac{\tilde{\omega}^2}{4\pi\epsilon_0}(\bar{\hat{\boldsymbol{s}}}\boldsymbol{\gamma}_{sN}(\bar{\boldsymbol{\kappa}},\omega) + \bar{\hat{\boldsymbol{p}}}_{N-}\boldsymbol{\gamma}_{pN}(\bar{\boldsymbol{\kappa}},\omega))\cdot\boldsymbol{\mu}^+(\omega)\frac{e^{i\tilde{\omega}n_N r}}{r}, \tag{47}$$

$$\boldsymbol{H}^+(\boldsymbol{r},\omega) \sim \frac{n_N c\tilde{\omega}^2}{4\pi}(\bar{\hat{\boldsymbol{s}}}\boldsymbol{\gamma}_{pN}(\bar{\boldsymbol{\kappa}},\omega) - \bar{\hat{\boldsymbol{p}}}_{N-}\boldsymbol{\gamma}_{sN}(\bar{\boldsymbol{\kappa}},\omega))\cdot\boldsymbol{\mu}^+(\omega)\frac{e^{i\tilde{\omega}n_N r}}{r}, \tag{48}$$

with

$$\begin{aligned}\boldsymbol{\gamma}_{sN}(\bar{\boldsymbol{\kappa}},\omega) &= \left(\frac{w_N T_{1N}^s e^{iw_1 d}}{w_1}\right)\hat{\boldsymbol{s}}, \\ \boldsymbol{\gamma}_{pN}(\bar{\boldsymbol{\kappa}},\omega) &= \left(\frac{w_N T_{1N}^p e^{iw_1 d}}{w_1}\right)\hat{\boldsymbol{p}}_{1-}.\end{aligned} \tag{49}$$

Here $\bar{\boldsymbol{\kappa}} = \tilde{\omega}n_N(\hat{\boldsymbol{x}}\hat{\boldsymbol{x}} + \hat{\boldsymbol{y}}\hat{\boldsymbol{y}}).\hat{\boldsymbol{r}}$, and the overbars again denote evaluation at $\bar{\boldsymbol{\kappa}}$. Similar to the calculations for the Stokes radiation in the cladding, we find the Stokes radiation per unit time per unit area in the substrate to be

$$\langle \boldsymbol{S}_S(\boldsymbol{r})\rangle = \frac{\tilde{\omega}_S^4 n_N(\omega_S)c}{32\pi^2\epsilon_0}(\alpha_1\ell_S)^2\frac{\hat{\boldsymbol{r}}}{r^2}\boldsymbol{\Gamma}_{\text{sub}}(\hat{\boldsymbol{r}},\omega_S) : (\boldsymbol{e}_L^*\boldsymbol{e}_L), \tag{50}$$

with

$$\boldsymbol{\Gamma}_{\text{sub}}(\hat{\boldsymbol{r}},\omega_S) = \boldsymbol{\gamma}_{sN}^*(\bar{\boldsymbol{\kappa}},\omega_S)\boldsymbol{\gamma}_{sN}(\bar{\boldsymbol{\kappa}},\omega_S) + \boldsymbol{\gamma}_{pN}^*(\bar{\boldsymbol{\kappa}},\omega_S)\boldsymbol{\gamma}_{pN}(\bar{\boldsymbol{\kappa}},\omega_S). \tag{51}$$

The normalized differential cross section in the substrate is then found to be

$$\bar{\sigma}_S(\hat{\boldsymbol{r}}) = \frac{3n_1(\omega_P)n_N(\omega_S)}{8\pi n_1(\omega_S)n_N(\omega_P)}\boldsymbol{\Gamma}_{\text{sub}}(\hat{\boldsymbol{r}},\omega_S) : (\boldsymbol{e}_L^*\boldsymbol{e}_L). \tag{52}$$

We can then find the azimuthally integrated differential cross section for the radiation into the substrate:

$$\begin{aligned}\bar{\sigma}_{\text{sub}}(\theta) = \frac{3}{8}\frac{n_1^P n_N}{n_1 n_N^P}\Bigg(& \left|\frac{w_N T_{1N}^s}{w_1}T_{N1}^{sP}F_s e^{i(w_1^P + w_1)d}\right|^2 \\ & + \left|\frac{w_N T_{1N}^s}{w_1}\frac{w_1^P}{\tilde{\omega}^P n_1^P}T_{N1}^{pP}F_p e^{i(w_1^P + w_1)d}\right|^2 \\ & + 2\left|\frac{w_N \kappa T_{1N}^p}{w_1\tilde{\omega}n_1}\frac{\kappa^P}{\tilde{\omega}^P n_1^P}T_{N1}^{pP}F_p e^{i(w_1^P + w_1)d}\right|^2 \\ & + \left|\frac{w_N T_{1N}^p}{\tilde{\omega}n_1}\frac{w_1^P}{\tilde{\omega}^P n_1^P}T_{N1}^{pP}F_p e^{i(w_1^P + w_1)d}\right|^2 \\ & + \left|\frac{w_N T_{1N}^p}{\tilde{\omega}n_1}T_{N1}^{sP}F_s e^{i(w_1^P + w)d}\right|^2\Bigg), \end{aligned} \tag{53}$$

where T_{1N}^s and T_{1N}^p are the Fresnel transmission coefficients from the cladding to the substrate. As it is expected, Eq. (53) shows that the cross section in the substrate depends on the fraction of the incident intensity transmitted through the structure from substrate to the cladding, multiplied by that fraction scattered through the structure from cladding to the substrate. The total Stokes cross section for radiation into the substrate is then

$$\bar{\sigma}_{\text{sub}}^{\text{tot}} = \int_{\pi/2}^{\pi} \bar{\sigma}_{\text{sub}}(\theta)\sin(\theta)\mathrm{d}\theta, \tag{54}$$

analogous to Eq. (46).

We are interested in structures that have poles in their Fresnel coefficients. For example, if the structure has a resonance at the Stokes frequency for *s* polarization, the transmission coefficient T^s_{1N} will have a pole at a complex wavenumber κ^S_{res}:

$$T^s_{1N} \sim \frac{\tau^S_{1N}}{\kappa - \kappa^S_{\mathrm{res}}}, \tag{55}$$

for κ close to $\kappa^S_R \equiv \mathrm{Re}(\kappa^S_{\mathrm{res}})$, where $\kappa^S_{\mathrm{res}} = \kappa^S_R + i\kappa^S_I$, and τ^S_{1N} is also in general a complex number. Thus (53) simplifies to

$$\bar{\sigma}_{\mathrm{sub}}(\theta) \sim \frac{3}{8}\frac{n_1^P n_N}{n_1 n_N^P}\left|\frac{w_N}{w_1}T^{sP}_{N1}e^{i(w_1^P + w_1)d}\right|^2 \times \frac{|\tau^S_{1N}|^2}{(\kappa - \kappa^S_R)^2 + (\kappa^S_I)^2}, \tag{56}$$

near the resonance. To calculate the contribution of the pole to $\bar{\sigma}^{\mathrm{tot}}_{\mathrm{sub}}$, we evaluate the slowly varying terms in Eq. (56) at $\theta_R = \sin^{-1}(\frac{\kappa^S_R}{\tilde{\omega} n_N})$, where the Lorentzian is centered, and integrate over the Lorentzian. The resonance contribution to the total Stokes cross section in the substrate becomes

$$\bar{\sigma}^{\mathrm{pole}}_{\mathrm{sub}} \simeq \frac{|\tan\,\theta_R|}{2n_N}\lambda\kappa^S_I\bar{\sigma}^{\mathrm{pole}}_{\mathrm{max}}, \tag{57}$$

where λ is the vacuum wavelength of the Stokes field and $\bar{\sigma}^{\mathrm{pole}}_{\mathrm{max}}$ comes from evaluating Eq. (56) at θ_R. Equations (56) and (57) show that the resonance contribution $\bar{\sigma}^{\mathrm{pole}}_{\mathrm{sub}}$ scales with the inverse of κ^S_I and, thus, is maximized by maximizing the propagation length ($(\kappa^S_I)^{-1}$) of the excitation signaled by the resonance [Eq. (55)]. We will see examples of this below.

3. SERS IN MULTILAYERED STRUCTURES

The approach presented in the previous section can be used to describe Raman scattering in an arbitrary planar structure. Here we are interested in the enhancement of the Raman scattering due to the resonant coupling of both pump and Stokes radiations into the guided modes of layered structures. In particular, we consider three types of guided modes: a BSW supported by a periodic multilayer, a WG mode supported by a slab WG, and an SP supported by a metal/dielectric interface. While our focus here is on dielectric structures, and it is well known that the Raman scattering from molecules at a smooth metal surface can be significantly enhanced by introducing roughness, we include the planar SP structure because such structures are of interest in sensing applications [2], and from the fundamental optics point of view.

We present example calculations for pumps at 532 and 1064 nm, and consider a Raman shift of 3000 cm^{-1} [42]. For the metal we choose gold. For the dielectric materials, we choose SiO_2 and Ta_2O_5. Commonly used in Raman filters, these dielectrics exhibit only a weak photoluminescence when pumped in the energy ranges of interest. We first consider semi-infinite versions of these structures, shown in Fig. 2, taking the cladding in all structures to be air.

The multilayer structure shown in Fig. 2(a) is a truncated 1D photonic crystal, with a unit cell composed of two layers of thicknesses $d_{SiO_2} = 153$ nm and $d_{Ta_2O_5} = 87$ nm, and two additional top layers of thicknesses $d^{\mathrm{top}}_{Ta_2O_5} = 10$ nm and $d^{\mathrm{top}}_{SiO_2} = 10$ nm. It supports an *s*-polarized BSW over a wide range of wavelengths that includes $\lambda = 532$ nm; the BSW dispersion relation and the band regions are shown in the figure, where the dependence of the refractive indices on the photon energy is taken into account [43]. While the position of the photonic bandgap is determined by the choice of the unit cell, the dispersion relation of the BSW depends mainly on the truncation of the photonic crystal, and it is very sensitive to the thickness of the two layers closest to the cladding. As expected, the BSW is found within the bandgap region and below the cladding (air) light line. Indeed, the mode is confined at the multilayer side by the photonic bandgap and at the cladding side by total internal reflection. We also consider a second structure, with a unit cell composed of two layers of thicknesses $d_{SiO_2} = 401$ nm and $d_{Ta_2O_5} = 223$ nm, and two top layers of $d^{\mathrm{top}}_{Ta_2O_5} = 65$ nm and $d^{\mathrm{top}}_{SiO_2} = 10$ nm; it supports an *s*-polarized BSW over a wide range of wavelengths that includes $\lambda = 1064$ nm.

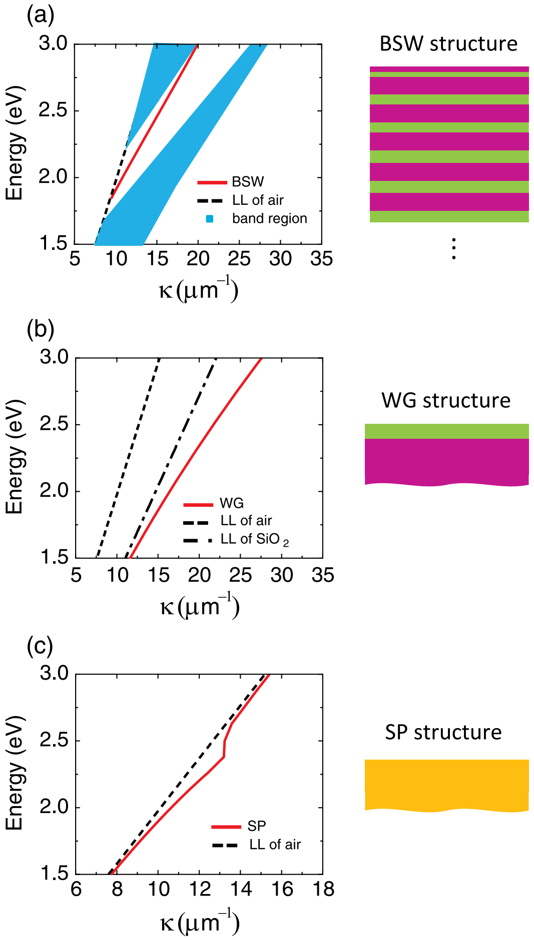

Fig. 2. (Color online) (a) BSW dispersion curve and cladding light line (LL) . (b) WG dispersion curve, cladding light line, and substrate light line. (c) SP dispersion curve and cladding light line.

The slab WG structures consist of SiO_2 covered with a single layer of Ta_2O_5; we choose a thickness of 100 nm for Ta_2O_5 for a pump at $\lambda = 532$ nm, and 200 nm for a pump at $\lambda = 1064$ nm. WGs are confined by total internal reflection from the cladding as well as from the underlying SiO_2; in Fig. 2(b) we show the dispersion relation of the *s*-polarized fundamental WG mode for the first of these two structures. As expected, it lies below the light lines of air and SiO_2.

The third system under investigation supports SPs that exist at a metal/dielectric interface. In this case, the SP dispersion relation is for the gold/air interface, and is shown in Fig. 2(c), where we have used Johnson and Christy's gold dielectric function [44], and plotted the real part of the SP wavenumber $\kappa = \tilde{\omega}\sqrt{\epsilon_m/(\epsilon_m+1)}$, where ϵ_m is the dielectric constant of the metal [2]. Here the confinement is due to total internal reflection from the cladding and the evanescent behavior in the metal resulting from the negative real part of the dielectric function.

It is worth noticing that BSW and WG dispersion relations can be adjusted on demand, by modifying the geometrical parameters of the structures. In contrast, the SP dispersion relation of the simple structure we have considered here is essentially determined by the dielectric function of the chosen materials.

A. Pump Intensity Enhancement

We now turn to the finite versions of these structures, which can be employed in sensing devices based on the Kretschmann geometry [26], as shown in Fig. 3. The prism material is chosen so that its light line lies to the right of the dispersion relation of the guided mode of interest. Thus the truly guided modes of the corresponding infinite systems become leaky, allowing coupling of pump radiation into and out of the modes through the prism.

From Eqs. (35) and (36) we see that, for a molecule at a distance d above a multilayer, the pump field amplitude depends on the s- and/or p-polarized Fresnel coefficients T_{N1}. In particular, when the structure supports a guided mode, such a transmission coefficient has a pole in the complex plane and an enhancement $|\mathcal{E}_L/\mathcal{E}|^2$ occurs as light incident from the prism is coupled into the mode through the prism. In Fig. 4 we plot this *pump enhancement factor* associated with the modes under investigation as a function of the detuning of the pump incident angle, θ_P, from θ_0, which is the coupling angle that corresponds to the maximum enhancement, and it is different in the three cases. Here we take $d = 1$ nm, a BK7 prism with index $n_{\text{prism}} = 1.5$ for the BSW and SP structures, and a gadolinium gallium garnet prism with $n = 1.98$ for the WG structures; note that the BK7 prism could not be used for the latter, since the effective indices of the guided modes are greater than 1.5. As a reference, we also indicate the pump enhancement factor in the cladding at $d = 1$ nm above a bare prism [Fig. 3(d)], where there is no mode. In all but the SP structure we consider s-polarized light.

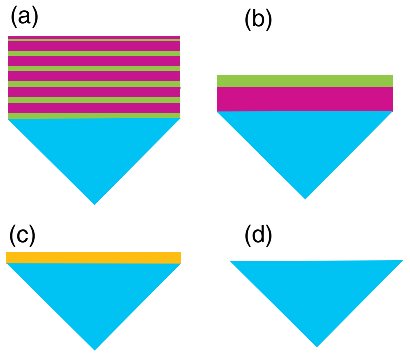

Fig. 3. (Color online) Structures: (a) multilayer structure with BSWs; (b) WG structure; (c) metallic structure with SP modes; (d) bare prism of the reference.

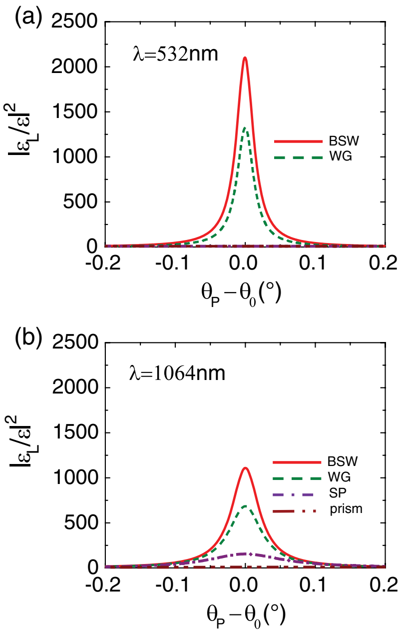

Fig. 4. (Color online) Pump enhancement factor for multilayer, WG, SP, and bare prism at (a) 532 and (b) 1064 nm. In (a), the very small rise in $|\mathcal{E}_L/\mathcal{E}|^2$ as $\theta \to \theta_0$ for the SP and bare prism structures cannot be seen.

The pump enhancement factor increases as the mode losses decrease. For the dielectric structures [Figs. 3(a) and 3(b)], where there is no absorption, and scattering losses due to fabrication imperfections are neglected, it diverges as the number of periods (thickness of the buffer layer) of the BSW structure (WG structure) increases, and the angular width of the peak tends to zero. In plotting Fig. 4 we have chosen 5(3) periods for the multilayer designed for 532 nm (1064 nm), and a buffer thickness of 340 nm (640 nm) for the WG designed for 532 nm (1064 nm). These parameters give $\Delta\kappa_{\text{res}} \simeq 20(\Delta\kappa_{2\text{ mm}})$, where $\Delta\kappa_{\text{res}}$ is the width of the resonance at the pump frequency, and $\Delta\kappa_{2\text{ mm}}$ is the spread in κ corresponding to an incident beam of width 2 mm; we confirm in Section 4 that the plane wave analysis we are pursuing here will be accurate for such a beam. For the SP structure we have chosen a metal thickness of 50 nm to maximize the pump enhancement factor at θ_0. The resonance is broader, and its width is determined both by absorption losses and coupling losses into the prism with the two contributions roughly equal. The SP structure shows a particularly poor enhancement at $\lambda = 532$ nm, due to large losses in the metal. These are reduced by working at longer wavelengths, but even at $\lambda = 1064$ nm the enhancement for the SP structure is smaller than that shown by the dielectric structures.

B. Stokes Radiation

As discussed in Section 2, the Raman scattering process can be treated as a two-step process: (i) the pump field at the position of the molecule induces a dipole moment proportional to the amplitude of the local field, and (ii) the Stokes field is radiated by the induced dipole. In the previous section, we showed that the incident field at the position of the molecule can be enhanced when a leaky mode is excited through the prism, and the appropriate T_{N1} at the pump frequency becomes large. To optimize the Raman signal, for each structure we choose a fixed incident angle at which the pump enhancement factor $|\mathcal{E}_L/\mathcal{E}|^2$ is maximized; here the induced dipole oscillates at its largest amplitude, and the dipole radiates everywhere into the cladding and substrate. From Eq. (53) we see that the Stokes radiation in particular directions in the substrate can be further enhanced if T_{1N} is large at the Stokes frequency, for example, in the presence of a leaky mode at that frequency; in this case, the Stokes radiation can resonantly couple through that mode before exiting through the prism. This kind of double enhancement has been studied in Brillouin scattering from metallic structures, where the Stokes shift is small [45]. The structures we have designed, and the choice of the proper prism, allow this "double resonance" condition for Stokes shifts up to 3000 cm^{-1}. In contrast, since there is no channel for the coupling of light from the modes into the cladding, there is no additional enhancement in Stokes or anti-Stokes radiation in that direction.

Calculations for the azimuthally integrated differential cross section for Stokes radiation into the substrate are shown in Fig. 5; note the logarithmic scale. For each structure there is a strong peak, corresponding to the coupling of the Stokes field to leaky modes. In addition, for the WG and BSW structures, other small peaks appear. These correspond to Fabry–Perot interferences, typical of a multilayered structure. The strong suppression of the Stokes signal around the BSW peak is due to the photonic bandgap, which attenuates the transmission of the Stokes radiation through the multilayer. The calculations show a maximum enhancement of about 6 and 5 orders of magnitude for the BSW and WG structures at 532 nm [Fig. 5(a)], and more than 4 orders of magnitude for the SP structures at 1064 nm [Fig. 5(b)].

It is interesting to consider $\bar{\sigma}_{\text{sub}}^{\text{tot}}$ [see Eq. (54)], the total normalized cross section for Raman radiation in the substrate. In a scenario where additional optical elements are used to collect the scattered light over a wide range of angles in the substrate, this would be the relevant parameter to characterize the overall enhancement of the collected Raman scattered light. In Fig. 6 we plot $\bar{\sigma}_{\text{sub}}^{\text{tot}}$ as a function of the distance d of the molecule from the surface of the structure; $\bar{\sigma}_{\text{sub}}^{\text{tot}}$ decreases as d increases, since at the significant κ all the fields in the cladding are evanescent. Note that the curves of the SP and bare prism structure are multiplied by 20. We can also find the contribution of the resonance coupling of the Stokes field to the total normalized Stokes cross section for scattering into the substrate using Eq. (57). While $\bar{\sigma}_{\text{sub}}^{\text{pole}}/\bar{\sigma}_{\text{sub}}^{\text{tot}}$ is only about 25% for the WG structures and about 60% for the BSW structures, it approaches 100% for the SP structures. Unlike the dielectric structures, in the metallic structures, radiation can propagate into the substrate only through the excitation of the SP, since the metal/air interface reflectivity is very high.

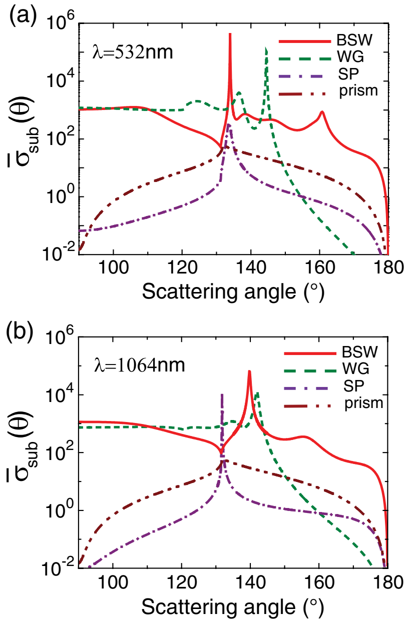

Fig. 5. (Color online) Differential cross sections normalized to the total cross section in free space ($n_1 = 1$) for the scattered field in the substrate: (a) $\lambda = 532$ nm; (b) $\lambda = 1064$ nm for multilayer, WG, SP, and bare prism structures.

The total normalized Raman cross section in the substrate and cladding add up to a value that is within a factor of 2 of the pump enhancement factor. Roughly speaking, this indicates that, although resonance coupling of the Stokes field results in large Stokes cross section in specific directions, the total Stokes cross section benefits only from the pump field resonance coupling, and light is redistributed only in space due to the Stokes resonance coupling. In the dielectric structures, only about 10% of the Stokes light is radiated into the cladding, because the coupling into the substrate through the dielectric structure is so effective. In the metallic structures, as discussed above, the Stokes radiation can reach the substrate only via coupling through the SP, and the rest of the radiation is necessarily reflected up into the cladding. Hence, in these structures, the Stokes radiation into the cladding is typically of the same order, or larger than, that reaching the substrate.

4. FINITE BEAM CORRECTIONS

In Subsection 2.B, we assumed the incident beam to be a plane wave [Eq. (34)] within our time window T. Taking $\boldsymbol{\kappa}^P$ to lie in the x direction and choosing a new set of directions identified by $(x'y'z')$, where z' indicates the direction in which the plane wave is propagating,

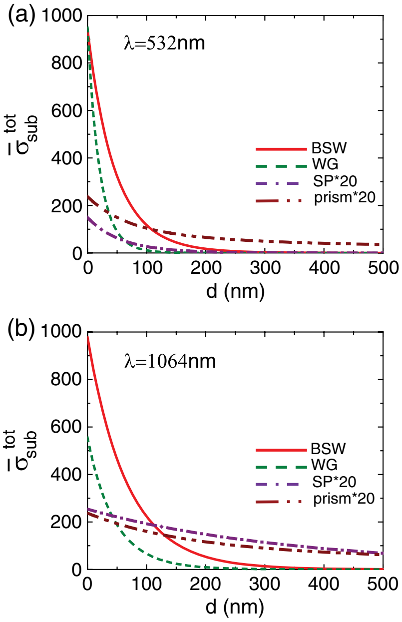

Fig. 6. (Color online) Integrated Raman cross section versus the distance of the molecule from the surface of the structure: (a) $\lambda = 532$ nm; (b) $\lambda = 1064$ nm for multilayer, WG, SP, and bare prism structures. The plots of SP and bare prism structures have been multiplied by 20.

$$\begin{cases} x' = -z \sin \theta_P + x \cos \theta_P, \\ y' = y, \\ z' = z \cos \theta_P + x \sin \theta_P, \end{cases} \tag{58}$$

(see Fig. 7), the field [Eq. (34)] can be written as $\boldsymbol{\mathcal{E}}_{\rm inc}(x',y',z')\exp(-i\omega_P t) + c.c.$, where $\boldsymbol{\mathcal{E}}_{\rm inc}(x',y',z') = \hat{\mathbf{s}}^P \mathcal{E}_{\rm inc}(x',y',z')$ if the incident plane wave is s polarized and $\boldsymbol{\mathcal{E}}_{\rm inc}(x',y',z') = \hat{\mathbf{p}}^P_{N+}\mathcal{E}_{\rm inc}(x',y',z')$ if it is p polarized, with

$$\mathcal{E}_{\rm inc}(x',y',z') = \mathcal{E} e^{i\nu_N^P z'} \tag{59}$$

actually depending only on z' and $\nu_N^P = \tilde{\omega}_P n_N$. In a more realistic treatment, we should consider a finite incident beam, which is a superposition of many plane waves with slightly different propagation directions and, therefore, slightly different wave vectors; this is particularly important for our dielectric structures, as they support very narrow resonant modes and, thus, coupling is possible in a very small angular range.

For the finite incident beam we use θ_P to indicate only the angle of incidence of the central wave vector in the superposition, which we now take to define the z' direction. Indeed, in moving from the field of an incident plane wave to the field of an incident finite beam resulting from such a superposition, Eq. (59) is replaced by an expression for the incident field that will depend on x' and y', as well as z'. We neglect the small differences between the polarization vectors of each component in the superposition, which we take to yield a finite beam that is approximately linearly polarized, and assume that the polarization direction of the full field can be approximated by either $\hat{\mathbf{s}}^P$ or $\hat{\mathbf{p}}^P_{N+}$ for the central component. For simplicity, we take the amplitude $\mathcal{E}_{\rm inc}(x',y',z')$ of the incident finite beam to be a Gaussian, given by

$$\mathcal{E}_{\rm inc}(x',y',z') = \mathcal{E} e^{i\nu_N^P z'} e^{-\frac{(x'^2+y'^2)}{2\Delta^2}}, \tag{60}$$

where Δ determines the width of the beam; this replaces the plane wave limit [Eq. (59)], and we have

$$\int |\mathcal{E}_{\rm inc}(x',y',z')|^2 \mathrm{d}x'\mathrm{d}y' = |\mathcal{E}|^2 \mathcal{A}, \tag{61}$$

where $\mathcal{A} = \pi\Delta^2$ is the effective area of the beam.

Using our original coordinate system, taking $E_{\rm inc}(x,y,z) = \mathcal{E}_{\rm inc}(x',y',z')$, we can write Eq. (60) as

$$E_{\rm inc}(x,y,0) = e^{i\nu_N^P x \sin\theta_P} \mathcal{E} f_{\rm inc}(x,y) \tag{62}$$

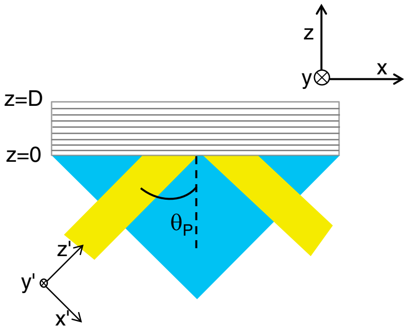

Fig. 7. (Color online) Finite beam of light incident on the multilayer structure, and its reflected beam.

along the plane $z = 0$, where

$$f_{\rm inc}(x,y) = e^{-\frac{x^2\cos^2\theta_P}{2\Delta^2}} e^{-\frac{y^2}{2\Delta^2}}. \tag{63}$$

The pump field driving the molecules is the field that results at $z = D + d$, but we first determine the field at $z = D^+$, which we denote by $E_{\rm clad}(x,y,D)$; as for $E_{\rm inc}(x,y,0)$, we approximately characterize its polarization by that of the central component, which will be either $\hat{\mathbf{s}}^P$ or $\hat{\mathbf{p}}^P_{1+}$, depending on whether the field is s- or p-polarized.

For the structures we study here, where a surface excitation exists in the limit of a semi-infinite structure, the Fresnel coefficient T^P_{N1} at the pump frequency has a pole at a complex wavenumber $\kappa^P_{\rm res}$:

$$T^P_{N1} \sim \frac{\tau^P_{N1}}{\kappa - \kappa^P_{\rm res}}, \tag{64}$$

when κ is close to $\kappa^P_R \equiv \mathrm{Re}(\kappa^P_{\rm res})$, and where τ^P_{N1} is also in general a complex number. We write $\kappa^P_{\rm res} = \kappa^P_R + i\kappa^P_I$, with κ^P_I describing the mode propagation losses due to absorption, if there are any, and the coupling to the substrate. This coupling will also slightly shift κ^P_R from the value for the real part of the surface excitation wavenumber in the limit of a semi-infinite structure. The values of $\kappa^P_{\rm res}$ and τ^P_{N1} can be extracted numerically from the full expression for T^P_{N1}; as well, semianalytic expressions can be constructed for them. To maximize the field enhancement in the cladding above the structure, we assume that θ_P is chosen such that $\nu^P_N \sin\theta_P = \kappa^P_R$. Then the field in the cladding just above the structure will be of the form

$$E_{\rm clad}(x,y,D) = e^{i\kappa^P_R x}\bar{E}_{\rm clad}(x,y,D),$$

where, within the approximation of Eq. (64), $\bar{E}_{\rm clad}(x,y,D)$ satisfies

$$\frac{\partial}{\partial x}\bar{E}_{\rm clad}(x,y,D) + \kappa^P_I \bar{E}_{\rm clad}(x,y,D) = i\tau^P_{N1}\mathcal{E} f_{\rm inc}(x,y) \tag{65}$$

for the incident field $E_{\rm inc}(x,y,0)$ of the form of Eq. (62) [46]; the solution of this equation can be written as

$$\bar{E}_{\rm clad}(x,y,D) = -\frac{\tau^P_{N1}}{i\kappa^P_I}\mathcal{E} f(x,y), \tag{66}$$

where

$$f(x,y) = \kappa^P_I \int_{-\infty}^{x} e^{-\kappa^P_I(x-x')} f_{\rm inc}(x',y)\mathrm{d}x'. \tag{67}$$

In the limit of a very broad beam ($\kappa^P_I\Delta \gg 1$), $f_{\rm inc}(x',y)$ varies little over the integration range, and we can write $f_{\rm inc}(x',y) \approx f_{\rm inc}(x,y) + (x'-x)(\frac{\partial f_{\rm inc}(x,y)}{\partial x}) + \ldots$ in Eq. (67), giving

$$f(x,y) \approx f_{\rm inc}(x,y) - (\kappa^P_I)^{-1}\frac{\partial f_{\rm inc}(x,y)}{\partial x} + \ldots \approx f_{\rm inc}(x - (\kappa^P_I)^{-1}, y). \tag{68}$$

The result is clearly more general than the particular form of Eq. (63), and holds whenever the propagation length $(\kappa^P_I)^{-1}$ is negligible compared to the beam width. Except for this small shift, we can obtain Eqs. (66) and (68) simply by assuming that, locally, the incident field can be treated as a plane wave, and putting $\bar{E}_{\rm clad}(x,y,D) = T_{N1}^{P}\mathcal{E}f_{\rm inc}(x,y)$ with T_{N1}^{P} given by Eq. (64) with $\kappa = \kappa_R^P$.

On the other hand, if the propagation length $(\kappa_I^P)^{-1}$ is much larger than the width Δ of the incident beam ($\kappa_I^P\Delta \ll 1$), in the integral in Eq. (67), we can expand the exponential about $x' = 0$, $\exp(-\kappa_I^P(x-x')) \approx \exp(-\kappa_I^P x)(1+\kappa_I^P x' + \ldots)$ and we find that $(\kappa_I^P)^{-1}$ sets the size of $f(x,y)$ in the x direction: we have $f(x,y) \approx 0$ for $x \ll \Delta$, and, for $x \gg \Delta$, we find

$$f(x,y) \to \frac{\sqrt{2\pi}\kappa_I^P\Delta}{\cos\theta_P} e^{-\frac{y^2}{2\Delta^2}} e^{-\kappa_I^P x}. \tag{69}$$

By using this in Eq. (66) we see that, in the x direction, $\bar{E}_{\rm clad}(x,y,D)$ extends over a range that is much larger than the distance characterizing the intersection of the beam with the plane $z = 0$.

In Figs. 8(a) and 8(c), we show the normalized intensity distribution, $|E_{\rm inc}(x,y,0)/\mathcal{E}|^2$, of an incident Gaussian beam characterized by FWHM of 2 mm and 50 μm, respectively. The light is incident from the substrate at an angle $\theta_P = 50.57°$ such that $\nu_N^P \sin\theta_P = \kappa_R^P$ for the BSW structure designed for use at $\lambda = 532$ nm; in Figs. 8(b) and 8(d), we show the corresponding normalized intensity distribution just above the structure in the cladding, $|E_{\rm clad}(x,y,D)/\mathcal{E}|^2$. For the 2 mm beam, the shape of the beam is not much distorted, suffering mainly a shift as discussed above. For this structure $\kappa_I^P \sim 6$ mm^{-1}, and the full range of wave vectors in the incident beam, characterized by $\Delta\kappa \approx (1/2$ mm$) = 0.5$ mm^{-1}, can couple into the BSW resonance; the field at the interface of the multilayer and the cladding is greatly enhanced. On the other hand, the 50 μm beam has a wider range of wavenumbers $\Delta\kappa \approx (1/50\ \mu$m$) = 20$ mm^{-1}, and not all can couple into the BSW resonance. The distance over x that $|f(x,y)|^2$ is substantial is now limited not by the width of the incident beam, but by the propagation length $(\kappa_I^P)^{-1} \gg \Delta$, as indicated by Eq. (69), and the enhancement is smaller.

As the field at the interface of the cladding and multilayer is modified compared to the limit of plane wave excitation, so will the prediction of the Raman signal change. For a molecule at position $\boldsymbol{r}_0 = (d+D)\hat{z} + \boldsymbol{R}_0$, we can immediately calculate this, since the total Stokes Raman light scattered by a molecule into the substrate depends on the pump field at the position of the molecule. Considering a finite incident beam, the Stokes radiation per unit time per unit area in the substrate is

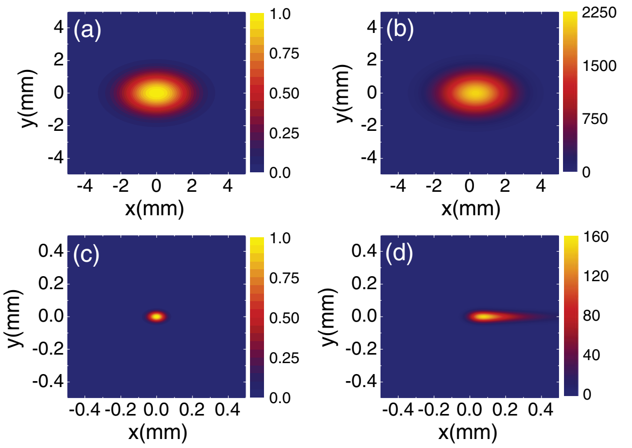

Fig. 8. (Color online) Normalized intensity distribution of incident beams at 532 nm with (a) 2 mm and (c) 50 μm FWHM, and (b) and (d) the corresponding intensity in the cladding for the BSW structure.

$$\langle \boldsymbol{S}_S(\boldsymbol{r})\rangle = \frac{\tilde{\omega}_S^4 n_N(\omega_S)c}{32\pi^2\epsilon_0}(\alpha_1\ell_S)^2\frac{\hat{\boldsymbol{r}}}{r^2}\boldsymbol{\Gamma}_{\rm sub}(\hat{\boldsymbol{r}},\omega_S)$$
$$:(\boldsymbol{e}'^{*}_L(x_0,y_0)\boldsymbol{e}'_L(x_0,y_0)), \tag{70}$$

[replacing Eq. (50)], where

$$\boldsymbol{e}'_L(x_0,y_0) = f(x_0,y_0)\boldsymbol{e}_L. \tag{71}$$

We neglect the small differences in the wave vector components of the incident beam and evaluate $\boldsymbol{e}_L$ (36) at $\kappa^P = \kappa_R^P$. For an ensemble of N molecules, uniformly distributed with an areal density ρ in a plane at $z = d + D$, the total Stokes radiation, $\langle \boldsymbol{S}_S^{\rm all}(\boldsymbol{r})\rangle$, is the sum of the radiation from all the individual molecules, since the spontaneous Raman scattering is an incoherent process. For a large number of molecules, we can convert the sum into an integral:

$$\langle \boldsymbol{S}_S^{\rm all}(\boldsymbol{r})\rangle = \rho\frac{\tilde{\omega}_S^4 n_N(\omega_S)c}{32\pi^2\epsilon_0}(\alpha_1\ell_S)^2\frac{\hat{\boldsymbol{r}}}{r^2}\boldsymbol{\Gamma}_{\rm sub}(\hat{\boldsymbol{r}},\omega_S)$$
$$:(\boldsymbol{e}_L^{*}\boldsymbol{e}_L)\times\int|f(x_0,y_0)|^2 {\rm d}x_0{\rm d}y_0. \tag{72}$$

To characterize the signal, we consider the ratio of the total power of the Stokes Raman light radiated into the substrate,

$$P_S = \int\langle \boldsymbol{S}_S^{\rm all}(\boldsymbol{r})\rangle\cdot\hat{\boldsymbol{r}}r^2{\rm d}\Omega, \tag{73}$$

to the incident pump power $P_{\rm pump} = S_p\mathcal{A}$, normalized to the Raman cross section in free space. This ratio can be written as

$$\frac{1}{\sigma_S^o}\frac{P_S}{P_{\rm pump}} = \rho\bar{\sigma}_{\rm sub}^{\rm tot}\frac{\int|f(x,y)|^2{\rm d}x{\rm d}y}{\mathcal{A}}, \tag{74}$$

with $\bar{\sigma}_{\rm sub}^{\rm tot}$ given by Eq. (54). In the limit of a very broad beam ($\kappa_I^P\Delta \gg 1$),

$$\frac{1}{\sigma_S^o}\frac{P_S}{P_{\rm pump}} \to \frac{\rho\bar{\sigma}_{\rm sub}^{\rm tot}}{\cos\theta_P},$$

and becomes constant and independent of the beam size. On the other hand, for a very small spot size ($\kappa_I^P\Delta \ll 1$),

$$\frac{1}{\sigma_S^o}\frac{P_S}{P_{\rm pump}} \to \frac{\sqrt{\pi}\rho\bar{\sigma}_{\rm sub}^{\rm tot}}{\cos^2\theta_P}\kappa_P^I\Delta,$$

exhibiting a linear dependence on the beam size, with a slope inversely proportional to the propagation length.

In Fig. 9, we have plotted the quantity in Eq. (74) (divided by ρ) for the bare prism, SP, WG, and BSW structures at 532 and 1064 nm (multiplied by 40 for the prism and SP structure) as the spot size varies. The bare prism does not have a resonant mode, and we cannot use the above pole expansion calculation. In this case, the beam undergoes a Goos–Hanchen

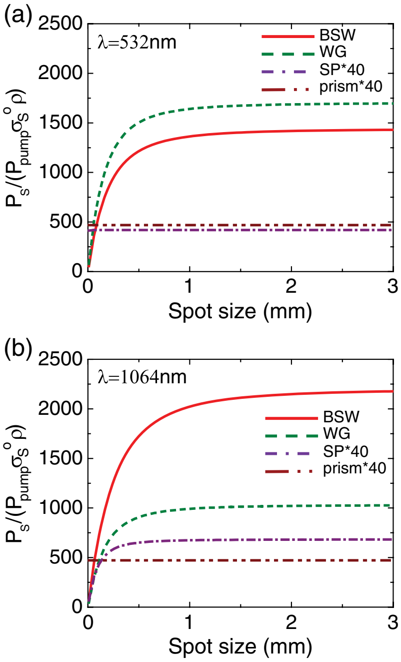

Fig. 9. (Color online) Normalized Raman scattering power per unit areal density of molecules, for the multilayer, WG, SP, and bare prism structures at (a) 532 and (b) 1064 nm. The plots of the SP and bare prism structures have been multiplied by 40.

shift, which is very small compared to the size of the beam. The other three structures support resonant modes and, therefore, we can use the pole analysis. For small spot sizes, as mentioned earlier, the coupling of the incident beam to the resonance mode is poor and, therefore, molecules on the surface feel a smaller field. In addition, a small spot size can illuminate only a small surface area of the structure and, therefore, the field scatters off only a small number of molecules, making the scattering signal small. On the contrary, as the spot size increases, both the number of illuminated molecules and the pump field coupling efficiency are larger, and therefore the Raman signal increases.

At 532 nm, the WG structure seems to enhance the Raman signal even more than the BSW structure. The reason is that, while the values of $\bar{\sigma}_{\text{sub}}^{\text{tot}}$ for the WG and BSW structures are very close (see Fig. 6), the integral in Eq. (74) depends on $1/\cos\theta_P$. The resonance angle of the WG structure is smaller than the one of the BSW structure, such that $1/\cos\theta_P$, when multiplied by $\bar{\sigma}_{\text{sub}}^{\text{tot}}$, becomes larger for the WG structure. At 1064 nm, $\bar{\sigma}_{\text{sub}}^{\text{tot}}$ of the WG structure is about half of the one of the BSW structure and, thus, it cannot be compensated by the slightly smaller resonance angle of the WG structure.

5. CONCLUSION

We have presented a systematic study of spontaneous Raman scattering for molecules on an arbitrary planar structure. The Raman cross sections for scattering into the cladding and substrate are expressed in terms of the Fresnel coefficients of the structure. This is particularly useful in studying Raman scattering in structures supporting guided modes, where the modes are signaled by poles in the Fresnel coefficients, and analytic expressions for the radiation through the guided modes to the substrate can be derived.

In comparing the Raman scattering of molecules on a planar structure supporting a guided mode to those in free space, we find that, in general, there is a twofold enhancement, with the Stokes cross section proportional to both pump and Stokes intensity enhancements. As long as there is a guided mode at the Stokes frequency, the differential cross section for scattering into the substrate exhibits a Lorentzian peak around a resonance polar angle, with an angular width depending on the propagation losses in the structure. For simplicity, we have assumed that the Raman polarizability tensor is isotropic; therefore, the dependence on the azimuthal angle is weak, and the Stokes intensity is peaked at the cross section of a cone defined by the Stokes resonance angle.

We have numerically calculated the differential Raman–Stokes cross sections for a set of multilayer structures, some supporting SPs, some WG modes, and some BSWs, with guided modes present in all cases at both pump and Stokes frequencies. For the SP structures, essentially all of the light radiated into the substrate is coupled through the SP resonance, where a maximum enhancement of more than 10^4 was found for excitation at 1064 nm. For the dielectric structures there is nonnegligible radiation into the substrate outside the resonance cone of the guided modes, but even so a maximum enhancement of about 10^6 was found for excitation of a BSW structure at 532 nm. The Stokes cross section, integrated over all angles, however, is enhanced by a smaller factor, up to 10 for the SP structures and up to 10^3 for the BSW structures. This is a result of the enhancement of the pump field, with the excitation of the guided modes at the Stokes frequency leading mainly to a redistribution in angle of the radiated power.

We have also confirmed that these results, initially derived from a plane wave analysis, survive the extension of the theory to treat the more realistic scenario of excitation by a finite pump beam, as long as that beam is of the order of millimeters in diameter. For smaller beam sizes, the coupling of the incident field to the guided mode is decreased, as is the number of molecules illuminated by the incident beam and, therefore, the power of the Stokes radiation is decreased.

The enhancements that we predict for the dielectric structures are still less than those reported in traditional SERS substrates of rough metal surfaces, or metal surfaces decorated with metallic nanoparticles. However, the dielectric structures do not suffer from absorption losses, and they offer the possibility of decoration with metallic nanoparticles to achieve larger cross sections despite the induced losses. The BSW structures also offer more freedom for design, and the possibility of tailoring the dispersion relation. The latter would be extremely important in an extension to treat coherent anti-Stokes Raman scattering, which would benefit from phase matching; we plan to turn to this in a future publication. Further, the confinement of BSWs into 1D channels is possible, when additional guiding structures are fabricated on a BSW structure [47,48]. This would lead to possibilities for multiplexed sensors, above and beyond the multiplexing that may be possible with the use of the Kretschmann configuration considered here.

ACKNOWLEDGMENTS

This work was supported in part by the Natural Sciences and Engineering Research Council of Canada Strategic Network for Bioplasmonic Systems (BiopSys), and Regione Lombardia through “Fondo per la promozione di accordi istituzionali Progetti di cooperazione scientifica e tecnologica internazionale” (Project code SAL-11).

REFERENCES

1. A. Campion and P. Kambhampati, “Surface-enhanced Raman scattering,” Chem. Soc. Rev. **27**, 241–250 (1998).
2. E. L. Ru and P. Etchegoin, *Principles of Surface-Enhanced Raman Spectroscopy: and Related Plasmonic Effects* (Elsevier Science 2008).
3. M. Moskovits, “Surface-enhanced spectroscopy,” Rev. Mod. Phys. **57**, 783–826 (1985).
4. M. Fleischmann, P. J. Hendra, and A. J. McQuillan, “Raman spectra of pyridine adsorbed at a silver electrode,” Chem. Phys. Lett. **26**, 163–166 (1974).
5. S. Lal, S. Link, and N. J. Halas, “Nano-optics from sensing to waveguiding,” Nat. Photon. **1**, 641–648 (2007).
6. H. Lin, J. Mock, D. Smith, T. Gao, and M. J. Sailor, “Surface-enhanced Raman scattering from silver-plated porous silicon,” J. Phys. Chem. B **108**, 1165–1167 (2004).
7. F. Giorgis, E. Descrovi, A. Chiodoni, E. Froner, M. Scarpa, A. Venturello, and F. Geobaldo, “Porous silicon as efficient surface enhanced Raman scattering (SERS) substrate,” Appl. Surf. Sci. **254**, 7494–7497 (2008).
8. A. Y. Panarin, S. N. Terekhov, K. I. Kholostov, and V. P. Bondarenko, “SERS-active substrates based on *n*-type porous silicon,” Appl. Surf. Sci. **256**, 6969–6976 (2010).
9. Y. F. Chan, H. J. Xu, L. Cao, Y. Tang, D. Y. Li, and X. M. Sun, “ZnO/Si arrays decorated by Au nanoparticles for surface enhanced Raman scattering study,” J. Appl. Phys. **111**, 033104 (2012).
10. S. Nie and S. R. Emory, “Probing single molecules and single nanoparticles by surface-enhanced Raman scattering,” Science **275**, 1102–1106 (1997).
11. K. Kneipp, Y. Wang, H. Kneipp, L. T. Perelman, I. Itzkan, R. R. Dasari, and M. S. Feld, “Single molecule detection using surface-enhanced Raman scattering (SERS),” Phys. Rev. Lett. **78**, 1667–1670 (1997).
12. W. L. Barnes, A. Dereux, and T. W. Ebbesen, “Surface plasmon subwavelength optics,” Nature **424**, 824–830 (2003).
13. N. Felidj, J. Aubard, G. Levi, J. R. Krenn, A. Hohenau, G. Schider, A. Leitner, and F. R. Aussenegg, “Optimized surface-enhanced Raman scattering on gold nanoparticle arrays,” Appl. Phys. Lett. **82**, 3095 (2003).
14. A. G. Brolo, E. Arctander, R. Gordon, B. Leathem, and K. L. Kavanagh, “Nanohole-enhanced Raman scattering,” Nano Lett. **4**, 2015–2018 (2004).
15. M. Kahl, E. Voges, S. Kostrewa, C. Viets, and W. Hill, “Periodically structured metallic substrates for SERS,” Sens. Actuators B **51**, 285–291 (1998).
16. X. Yang, C. Shi, D. Wheeler, R. Newhouse, B. Chen, J. Z. Zhang, and C. Gu, “High-sensitivity molecular sensing using hollow-core photonic crystal fiber and surface-enhanced Raman scattering,” J. Opt. Soc. Am. A **27**, 977–984 (2010).
17. J. F. Rabolt, “Waveguide Raman spectroscopy in the near infrared,” in *Fourier Transform Raman Spectroscopy from Concept to Experiment*, J. F. Rabolt and D. B. Chase, eds. (Academic, 1994), pp. 133–156.
18. J. F. Rabolt and J. D. Swalen, “Structure and orientation in thin films: Raman studies with integrated optical techniques,” in *Spectroscopy of Surfaces*, R. J. H. Clark and R. E. Hester, eds., Vol. **16** of Advances in Spectroscopy (Wiley, 1988), pp. 1–36.
19. L. Kang and R. E. Dessy, “Slab waveguide in chemistry,” Crit. Rev. Anal. Chem. **21**, 377–388 (1990).
20. Y. Levy, C. Imbert, S. Cipriani, S. Racine, and R. Dupeyrat, “Raman scattering of thin films as a waveguide,” Opt. Commun. **11**, 66–69 (1974).
21. J. F. Rabolt, R. Santo, and J. D. Swalen, “Raman measurements on thin polymer films and organic monolayers,” Appl. Spectrosc. **34**, 517–521 (1980).
22. J. S. Kanger, C. Otto, M. Slotboom, and J. Greve, “Waveguide Raman spectroscopy of thin polymer layers and monolayers of biomolecules using high refractive index waveguides,” J. Phys. Chem. **100**, 3288–3292 (1996).
23. A. Pope, A. Schulte, Y. Guo, L. K. Ono, B. R. Cuenya, C. Lopez, K. Richardson, K. Kitanovski, and T. Winningham, “Chalcogenide waveguide structures as substrates and guiding layers for evanescent wave Raman spectroscopy of bacteriorhodopsin,” Vibr. Spectrosc. **42**, 249–253 (2006).
24. G. Stanev, N. Goutev, and Zh. S. Nickolov, “Coupled waveguides for Raman studies of thin liquid films,” J. Phys. D **31**, 1782–1786 (1998).
25. A. Otto, “Excitation of nonradiative surface plasma waves in silver by the method of frustrated total reflection,” Z. Phys. **216**, 398–410 (1968).
26. E. Kretschmann and H. Raether, “Radiative decay of nonradiative surface plasmons excited by light,” Z. Naturforsch. A **23**, 2135–2136 (1968).
27. J. Homola, “Present and future of surface plasmon resonance biosensors,” Anal. Bioanal. Chem. **377**, 528–539 (2003).
28. Raman scattering in the Kretschmann configuration employing surface plasmon structures was discussed by J. Giergiel, E. Reed, J. C. Hemminger, and S. Ushioda, “Surface plasmon polariton enhancement of Raman scattering in Kretschmann geometry,” J. Phys. Chem. **92**, 5357–5365 (1988).
29. A. Yariv and P. Yeh, *Optical Waves in Crystals* (Wiley, 2003).
30. P. Yeh, A. Yariv, and A. Y. Cho, “Optical surface waves in periodic layered media,” Appl. Phys. Lett. **32**, 104–105 (1978).
31. M. Liscidini and J. E. Sipe, “Analysis of Bloch surface waves assisted diffraction-based biosensors,” J. Opt. Soc. Am. B **26**, 279–289 (2009).
32. M. Liscidini, M. Galli, M. Shi, G. Dacarro, M. Patrini, D. Bajoni, and J. E. Sipe, “Strong modification of light emission from a dye monolayer via Bloch surface waves,” Opt. Lett. **34**, 2318–2320 (2009).
33. M. Shinn and W. M. Robertson, “Surface plasmon-like sensor based on surface electromagnetic waves in a photonic bandgap material,” Sens. Actuators B **105**, 360–364 (2005).
34. F. Giorgis, E. Descrovi, C. Summonte, L. Dominici, and F. Michelotti, “Experimental determination of the sensitivity of Bloch surface waves based sensors,” Opt. Express **18**, 8087–8093 (2010).
35. V. Paeder, V. Musi, L. Hvozdara, S. Herminjard, and H. P. Herzig, “Detection of protein aggregation with a Bloch surface wave based sensor,” Sens. Actuators B **157**, 260–264 (2011).
36. H. Qiao, B. Guan, J. J. Gooding, and P. J. Reece, “Protease detection using a porous silicon based Bloch surface wave optical biosensor,” Opt. Express **18**, 15174–15182 (2010).
37. E. Guillermain, V. Lysenko, and T. Benyattou, “Surface wave photonic device based on porous silicon multilayers,” J. Lumin. **121**, 319–321 (2006).
38. J. D. Jackson, *Classical Electrodynamics Third Edition* (Wiley, 1999).
39. R. Loudon, *The Quantum Theory of Light* (Oxford University, 2000).
40. J. E. Sipe, “The dipole antenna problem in surface physics: a new approach,” Surf. Sci. **105**, 489–504 (1981).
41. A. Yariv and P. Yeh, *Photonics: Optical Electronics in Modern Communications* (Oxford University, 2006).
42. R. L. McCreer, *Raman Spectroscopy for Chemical Analysis* (Wiley, 2000).
43. J. A. Woollam Inc., WVASE Software Manual.
44. P. B. Johnson and R. W. Christy, “Optical constants of the noble metals,” Phys. Rev. B **6**, 4370–4379 (1972).
45. W. M. Robertson, A. L. Moretti, and R. Bray, “Surface-plasmon-enhanced Brillouin scattering on silver films: double-resonance effect,” Phys. Rev. B **35**, 8919–8928 (1987).
46. J. E. Sipe and J. Becher, “Surface energy transfer enhanced by optical cavity excitation: a pole analysis,” J. Opt. Soc. Am. **72**, 288–295 (1982).
47. T. Sfez, E. Descrovi, L. Yu, D. Brunazzo, M. Quaglio, L. Dominici, W. Nakagawa, F. Michelotti, F. Giorgis, O. J. F. Martin, and H. P. Herzig, “Bloch surface waves in ultrathin waveguides: near-field investigation of mode polarization and propagation,” J. Opt. Soc. Am. B **27**, 1617–1625 (2010).
48. M. Liscidini, D. Gerace, D. Sanvitto, and D. Bajoni, “Guided Bloch surface wave polaritons,” Appl. Phys. Lett. **98**, 121118 (2011).